

# Lawrence Berkeley National Laboratory

## LBL Publications

### Title

Wettability and Flow Rate Impacts on Immiscible Displacement: A Theoretical Model

### Permalink

<https://escholarship.org/uc/item/5r948952>

### Journal

Geophysical Research Letters, 45(7)

### ISSN

0094-8276

### Authors

Hu, Ran  
Wan, Jiamin  
Yang, Zhibing  
[et al.](#)

### Publication Date

2018-04-16

### DOI

10.1002/2017gl076600

Peer reviewed



## RESEARCH LETTER

10.1002/2017GL076600

## Key Points:

- A theoretical model is proposed to describe the crossover from fingering to stable flow as a function of contact angle and capillary number
- The phase diagram predicted by the model shows that decreasing contact angle  $\theta$  stabilizes the displacement for  $\theta \geq 45^\circ$
- The extended phase diagram also captures the boundary between corner flow and cooperative filling for contact angle smaller than  $45^\circ$

## Supporting Information:

- Supporting Information S1
- Movie S1
- Movie S2
- Movie S3
- Movie S4
- Movie S5
- Movie S6

## Correspondence to:

Y.-F. Chen,  
csyfchen@whu.edu.cn

## Citation:

Hu, R., Wan, J., Yang, Z., Chen, Y.-F., & Tokunaga, T. (2018). Wettability and flow rate impacts on immiscible displacement: A theoretical model. *Geophysical Research Letters*, 45, 3077–3086. <https://doi.org/10.1002/2017GL076600>





Received 25 JUN 2017

Accepted 19 FEB 2018

Accepted article online 27 FEB 2018

Published online 2 APR 2018

## Wettability and Flow Rate Impacts on Immiscible Displacement: A Theoretical Model

Ran Hu<sup>1</sup> , Jiamin Wan<sup>2</sup> , Zhibing Yang<sup>1</sup>, Yi-Feng Chen<sup>1</sup> , and Tetsu Tokunaga<sup>2</sup> <sup>1</sup>State Key Laboratory of Water Resources and Hydropower Engineering Science, Wuhan University, Wuhan, China,<sup>2</sup>Energy Geosciences Division, Lawrence Berkeley National Laboratory, Berkeley, CA, USA

**Abstract** When a more viscous fluid displaces a less viscous one in porous media, viscous pressure drop stabilizes the displacement front against capillary pressure fluctuation. For this favorable viscous ratio conditions, previous studies focused on the front instability under slow flow conditions but did not address competing effects of wettability and flow rate. Here we study how this competition controls displacement patterns. We propose a theoretical model that describes the crossover from fingering to stable flow as a function of invading fluid contact angle  $\theta$  and capillary number  $Ca$ . The phase diagram predicted by the model shows that decreasing  $\theta$  stabilizes the displacement for  $\theta \geq 45^\circ$  and the critical contact angle  $\theta_c$  increases with  $Ca$ . The boundary between corner flow and cooperative filling for  $\theta < 45^\circ$  is also described. This work extends the classic phase diagram and has potential applications in predicting CO<sub>2</sub> capillary trapping and manipulating wettability to enhance gas/oil displacement efficiency.

## 1. Introduction

The displacement of fluid by another immiscible one in porous media is a phenomenon of great importance in a variety of natural, engineering, and industrial processes, including geological CO<sub>2</sub> sequestration (Benson & Cole, 2008), enhanced oil/gas recovery (Mason & Morrow, 2013), and fuel cells (Anderson et al., 2010). A common phenomenon in two-phase flow is the instability of displacement front, which affects the CO<sub>2</sub> storage capacity and gas/oil recovery efficiency. When the gravity is negligible, the fluid-fluid displacement is governed by the competition between the capillary force and viscous force. This competition is complicated by the pore surface's wettability, and consequently, the immiscible displacement pattern can range from capillary fingering and viscous fingering to a stable/compact front (Lenormand et al., 1988; Trojer et al., 2015; Zhang et al., 2011; Zheng et al., 2017). In the drainage processes in which a nonwetting fluid (invading fluid contact angle  $\theta > 90^\circ$ ) displaces a wetting fluid, Lenormand et al. (1988) proposed the classic phase diagram to distinguish displacement patterns via two dimensionless parameters: the capillary number  $Ca$  and the viscosity ratio  $M$ . Here  $Ca = v_i \mu_i / \sigma$  and  $M = \mu_i / \mu_d$ , in which  $\mu_i$  and  $v_i$  are, respectively, the viscosity and the characteristic velocity of the invading fluid,  $\sigma$  is the interfacial tension, and  $\mu_d$  is the viscosity of the defending fluid. Although a  $\cos \theta$  term can be included in the denominator of the capillary number (Cao et al., 2016; Jamaloei et al., 2012), it cannot quantitatively account for the impact of wettability on the immiscible displacement patterns in porous media (Trojer et al., 2015) because accurate scaling of capillary displacement with  $\cos \theta$  is strictly limited to straight capillaries (Anderson, 1986; Philip, 1971).

The challenge in describing the impact of wettability on the displacement patterns in porous media is how to link the local pore-scale filling events governed by the Young-Laplace law to the regional cooperative and/or competitive filling behavior. In capillary-dominated displacement, Cieplak and Robbins (1988, 1990) proposed three modes of meniscus motion (burst, touch, and overlap) to capture the effect of wettability on the fluid invasion morphology. They found that as the pore surface becomes more and more wet to the invading phase ( $\theta$  decreases), the typical width of fingers increases and appears to diverge at a critical contact angle  $\theta_c$ . In the spirit of Cieplak and Robbins model, extensive studies followed with focus on the evaporation processes (Chapuis et al., 2008; Chraïbi et al., 2009), the square network (Koiller et al., 1992), disordered (Jung et al., 2016), and 3-D porous media (Singh et al., 2017). Jung et al. (2016) conducted micromodel experiments with  $\theta$  ranging from  $46^\circ$  to  $180^\circ$  and found a consistent crossover from stable invasion to capillary fingering in the range of  $80^\circ < \theta < 120^\circ$ . A similar conclusion was reported in 3-D porous media experiments characterized with X-ray microtomography (Singh et al., 2017). These studies provide insights

into how wettability of pore surfaces impacts fluid invasion morphology via local menisci instability in the capillary-dominated flow regime, but the effect of the viscous force on the displacement pattern was not considered.

Under high flow rates, the viscous force plays a role in the fluid invasion processes and the displacement front propagation depends highly on the viscous ratio  $M$ . When a less viscous fluid displaces a more viscous one ( $M < 1$ ), the viscous force acting against the capillary force produces unstable fronts, and the resulted pattern formation is sensitive to the wettability. Holtzman and Segre (2015) proposed a novel pore-scale model to explore the interplay between viscosity, capillarity, and the wettability properties in cases with  $M < 1$ , indicating that the increase of  $Ca$  enhances viscous fingering regardless of wettability. This is because at high flow rates the meniscus instability of bursts is almost independent of the contact angle, and the instability stimulates the viscous-fingering flow pattern. The impact of wettability on immiscible displacement has also been observed in glass beads-filled Hele-Shaw experiments (Trojer et al., 2015) and in patterned microfluidic systems (Zhao et al., 2016). These studies indicate that decreasing the invading fluid contact angle in the range of  $180^\circ > \theta > \theta_c$  (i.e., from strong drainage to weak imbibition) stabilizes the displacement patterns, but the wettability effect is suppressed as flow rate increases.

Compared to the achievements in understanding wettability impacts in the limit of slow and unfavorable displacement conditions, less progress has been made in examining favorable displacement conditions ( $M > 1$ ). Under favorable displacement conditions, the viscous pressure field resides behind the displacement front and the interface is stable against the capillary pressure fluctuations that roughen the interface (He et al., 1992; Wong, 1994). Since the role of the viscous force at the interface is stabilization in the case of  $M > 1$ , and different from that in the case of  $M < 1$ , the mechanism of wettability together with the flow rate controlling the invasion morphology cannot be captured by existing models (Holtzman & Segre, 2015). Therefore, how wettability and flow rate control the immiscible displacement under favorable conditions needs to be further investigated.

The impact of wettability on the immiscible displacement patterns under the favorable displacement conditions plays a key role in the geological  $\text{CO}_2$  sequestration. During the postinjection stage, brine displaces the previously injected  $\text{CO}_2$ . Since the viscosity of brine is higher than that of supercritical ( $\text{scCO}_2$ ), the displacement front tends to become compact and stable as flow rate increases. However, change in wettability of rock surfaces resulting from the sorption of natural organic matter and hydrocarbons, or the long-term exposure to  $\text{CO}_2$  (El-Maghraby & Blunt, 2013; Iglauer et al., 2015; Kim et al., 2012) significantly affects the stability of displacement fronts and directly impacts the  $\text{scCO}_2$  capillary trapping (Chaudhary et al., 2013; Hu et al., 2017a). Therefore, quantifying the competing effects of wettability and flow rate on the displacement front instability during the postinjection stage becomes a critical issue to be addressed.

Here we investigate how the competing effects of wettability and flow rate control the fluid invasion processes under favorable displacement conditions. We propose a model for capturing the crossover from fingering to stable flow to elucidate the competing effects. Our work extends the classic phase diagram in the limits of drainage (Lenormand et al., 1988; Zhang et al., 2011) and imbibition conditions (Lenormand, 1990), and also explores the controls of wettability and flow rate on the transition of displacement fronts from fingering to stable under favorable displacement conditions.

## 2. Crossover From Capillary Fingering to Stable Displacement

### 2.1. Pore-Scale Simulation

We study the immiscible displacement by performing simulations of the Navier-Stokes equations with OpenFOAM (Greenshields, 2015). The pore network is constructed by placing circles on a triangular lattice  $(x_0, y_0)$  with a constant space  $a_0$  and specifying random center coordinate  $(x_i, y_i)$  and random radius  $(r_i)$  of circles, where  $a_0 = 600 \mu\text{m}$ ,  $r_0 = 285 \mu\text{m}$  (supporting information Figure S1). The length and width of the pore network are  $L = 20 \text{ mm}$  and  $W = 10 \text{ mm}$ , respectively. The porosity  $\phi$  is 0.261, and the pore volume is  $2.10 \mu\text{L}$ . The construction leads to some overlaps of the neighboring circles (posts) and result in some "dead" pores. The overlap is considered in this work to simulate the effects of grain consolidation in sintered bead packs and sandstone (Cieplak & Robbins, 1990). The pore network is fully saturated with  $\text{scCO}_2$  and then brine is injected with constant flow rates  $Q$ , with  $-5.04 \leq \log_{10} Ca \leq -2.74$ , where  $Ca = Q\mu_i/(A_c\sigma)$ ,  $A_c$  is the cross-sectional area of the inlet. The viscosity  $\mu$  and the density  $\rho$  of brine and  $\text{scCO}_2$  are, respectively,  $\mu_{\text{brine}} = 5.972 \times 10^{-4} \text{ Pa}\cdot\text{s}$ ,  $\mu_{\text{scCO}_2} = 2.276 \times 10^{-5} \text{ Pa}\cdot\text{s}$ ,  $\rho_{\text{brine}} = 993.9 \text{ kg/m}^3$ , and  $\rho_{\text{scCO}_2} = 281.8 \text{ kg/m}^3$  and  $\sigma = 3.3 \times 10^{-2}$

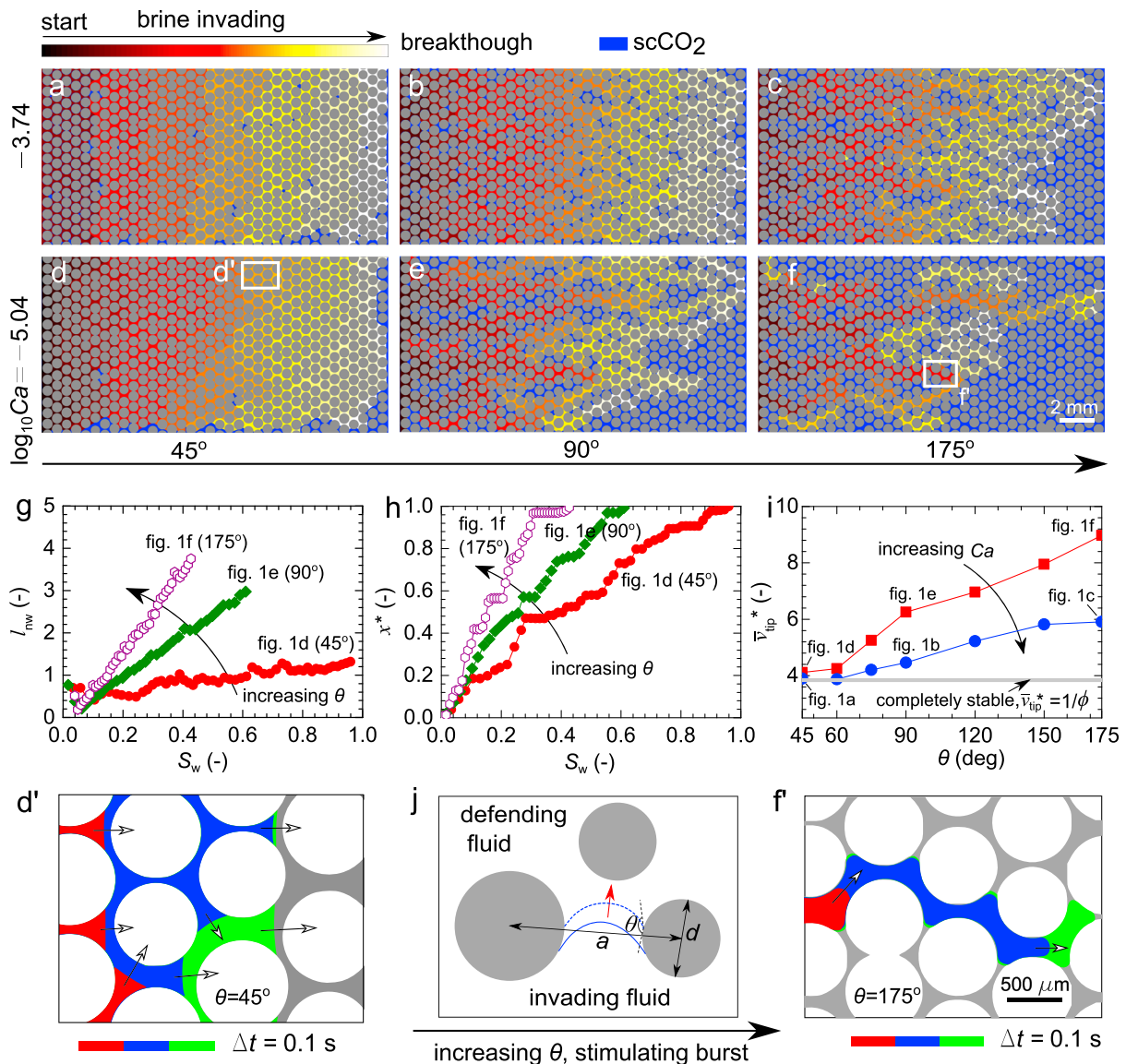


**Figure 1.** Evolution of the fluid-fluid displacement fronts with time for the imbibition (a, d), neutral (b, e), and drainage (c, f) processes under the intermediate (a–c) and lowest (d–f) flow rate conditions. These patterns (a–f) are characterized by the evolution of (g) the normalized fluid-fluid interface length  $l_{nw}^*$  and (h) the normalized displacement front  $x_{tip}^*$  with the invading fluid saturation  $S_w$ , and (i) the characteristic displacement front velocity  $\bar{v}_{tip}^*$  as a function of  $\theta$ . Also shown are the enlarged images (d', f') of the selected regions from (d) and (f). The water menisci advance at a time interval of 0.1 s during which 0.01 pore volume of brine is injected into the micromodel. The arrow indicates the direction of meniscus movement. The burst mode for the meniscus motion at the pore scale is given in (j).

N/m (Hu et al., 2017b). We simulate a total of 42 computational cases for the heterogeneous micromodel, with  $\log_{10}Ca = -5.04, -4.74, -4.04, -3.74, -3.04$ , and  $-2.74$  and  $\theta = 45^\circ, 60^\circ, 75^\circ, 90^\circ, 120^\circ, 150^\circ$ , and  $175^\circ$ . Detailed descriptions of simulations are included in supporting information Text S1 and Figure S1.

Figures 1a–1f present the evolution of the fluid-fluid displacement front at the lowest  $Ca$  (Figures 1d–1f,  $\log_{10}Ca = -5.04$ ) and at the capillary number of  $\log_{10}Ca = -3.74$ . The displacement patterns for the range of  $\theta$  and  $Ca$  presented in Figure 1 and SI Figure S2 show that the increase of  $\theta$  destabilizes the invasion morphology, shifting from stable at imbibition ( $\theta = 45^\circ$ ) to fingering at drainage ( $\theta = 175^\circ$ ). However, as  $Ca$  increases up to the highest  $Ca$  ( $\log_{10}Ca = -2.74$ ), fluid invasion is stable for all  $\theta$ , indicating that the impact of wettability on the fluid invasion processes becomes negligible, consistent with previous experimental and numerical results (Herring et al., 2015; Holtzman & Segre, 2015).

To gain an insight into the invasion processes, we plot the evolution of the fluid-fluid displacement fronts for imbibition (Figures 1a and 1d), neutral (Figures 1b and 1e) and drainage (Figures 1c and 1f) conditions, respectively. We characterize these patterns via the normalized fluid-fluid interface length  $l_{nw}$  (Figure 1g), the normalized displacement front location  $x_{tip}^*$  (Figure 1h), and the characteristic front velocity  $\bar{v}_{tip}^*$  (Figure 1i), with  $l_{nw} = L_{nw}/W$  and  $x_{tip}^* = x/L$ , where  $L_{nw}$  is the fluid-fluid interface length and  $x$  is the distance from the front tip to the inlet. The smooth fluid-fluid interface provides  $l_{nw} \approx 1$ ; and the larger the magnitude of  $l_{nw}$  is, the more irregular is the interface. For imbibition ( $\theta = 45^\circ$ , Figures 1a and 1d), the displacement is stable with  $l_{nw}$  almost remaining constant during the whole invasion processes (Figure 1g), whereas  $l_{nw}$  increases with a highest growth rate at  $\theta = 175^\circ$ , which indicates a highly fingered displacement pattern. The  $x_{tip}^*-S_w$  curves (Figure 1h) illustrate how displacement front advances toward the outlet, which was introduced to classify the capillary-/viscous-fingering regimes (Chen et al., 2017; Tsuji et al., 2016; Yamabe et al., 2015). A higher slope of the  $x_{tip}^*-S_w$  curves means a higher front velocity that leads to early breakthrough with less efficient displacement. To quantify the displacement front velocity during the whole invasion processes, we introduce a characteristic dimensionless front velocity  $\bar{v}_{tip}^*$  by averaging the dimensionless front velocity  $v_{tip}^*(t^*) = \partial x_{tip}^*/\partial t^*$  over the whole processes, where  $t^* = tQ/(LWh_0)$  is the scaled time,  $Q$  is the flow rate, and  $h_0$  is the depth of the pore network,  $h_0 = 40 \mu\text{m}$ . An analytical expression can be derived (supporting information Text S2):

$$\bar{v}_{tip}^* = \lim_{N \rightarrow \infty} \frac{1}{N} \sum_{i=1}^N v_{tip}^*(t_i^*) = \frac{1}{\phi S_{wb}}, \quad (1)$$

where  $S_{wb}$  is the invading fluid saturation at the breakthrough time.

Equation (1) shows that  $\bar{v}_{tip}^*$  is inversely proportional to the invading fluid saturation  $S_{wb}$  at the breakthrough time. For completely stable flow,  $S_{wb} = 1$ , and  $\bar{v}_{tip}^*$  approaches the minimum value of  $\bar{v}_{tip}^* = 1/\phi$ , while  $\bar{v}_{tip}^*$  increases as the displacement pattern shifts from stable to fingering flow. As shown in Figure 1i, for  $\theta < 60^\circ$ ,  $\bar{v}_{tip}^*$  almost remains constant at  $1/\phi$ , indicating that the corresponding displacements are stable. For  $\theta > 60^\circ$ ,  $\bar{v}_{tip}^*$  increases with  $\theta$  and the slope of  $\bar{v}_{tip}^*-\theta$  curve is smaller for higher  $Ca$ , demonstrating the stabilizing effect induced by the viscous pressure drop. For  $\log_{10} Ca = -5.04$ , the displacement pattern shifts from stable to fingering flow in the range of  $\theta = 60^\circ$  and  $90^\circ$  (supporting information Figure S2). This is consistent with Figure 1i which shows significant increases of  $\bar{v}_{tip}^*$  between  $\theta = 60^\circ$  and  $90^\circ$ .

The menisci motion at the pore scale controls the fluid-fluid interface instability at the pore network scale. As shown in Figure 1d' (selected region in Figure 1d), at small contact angle  $\theta = 45^\circ$ , two or more neighboring water menisci overlap and merge into a new one, leading to a smooth displacement front at the pore network scale (Jung et al., 2016; Zhao et al., 2016). However, under drainage condition, a single meniscus (Figure 1f', selected region in Figure 1f) advances independently of the neighboring water menisci, which can be represented by the burst mode (Cieplak & Robbins, 1988, 1990). The increase of  $\theta$  stimulates the burst events and hence leads to an unstable interface, but the destabilizing effect would be suppressed by viscous pressure drop.

## 2.2. A Theoretical Model

To quantify the interplay between wettability and flow rate, we consider the viscous pressure drop along the bulk flow direction that stabilizes the interface and the capillary pressure fluctuations (which lead to meniscus instabilities, i.e., bursts). The viscous pressure drop  $\delta P_v$  along the distance of  $\delta x$  can be written as (Homsy, 1987):

$$\delta P_v \sim (\mu_d - \mu_i) \frac{U}{K} \delta x, \quad (2)$$

where  $U$  is the velocity of the invading fluid, and  $K$  is the permeability of the medium. Since  $\mu_i > \mu_d$  during brine flooding, the pressure drop given by equation (2) yields  $\delta P_v < 0$ , and hence any small perturbation diminishes, resulting in a stable interface.

For the burst event in 2-D systems where the thin film is not considered, if the pressure drop between the two phases is larger than the maximum capillary pressure, no stable arc-shaped interface connecting to the two disks can exist (Figure 1j). The critical capillary force  $\delta P_{cr}$  corresponding to the minimum (critical) curvature

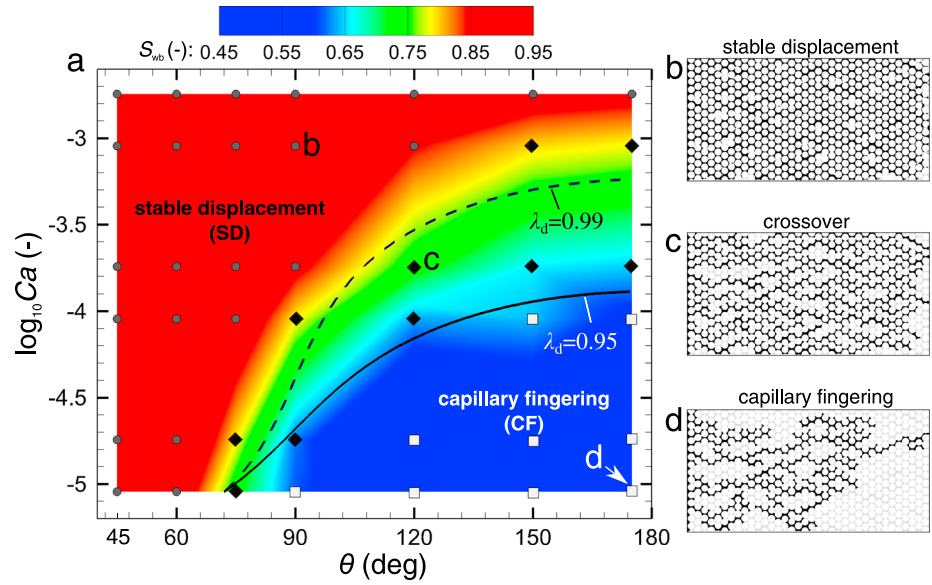


**Figure 2.** Phase diagram in the  $\theta$ - $\log_{10}Ca$  plane with  $\theta$  ranging from  $45^\circ$  to  $175^\circ$  under the favorable displacement conditions ( $M > 1$ ). The theoretical model predicts the crossover ( $\theta_c, Ca_c$ ) from capillary fingering to stable displacement with the characteristic length  $\lambda_d = 0.95$  (solid curve) and  $\lambda_d = 0.99$  (dashed curve). The dots represent the numerical conditions. The displacement patterns can be classified into a capillary fingering regime (square), a stable displacement regime (circle), and a crossover zone (diamond). The red color represents higher-invading fluid saturation  $S_{wb}$  at the breakthrough time, whereas the blue color represents lower-invading fluid saturation. The values of  $S_{wb}$  under all of the numerical conditions are listed in supporting information Table S1.

$R_c = \frac{a}{2} \cdot \left( \sqrt{1 - \lambda_d^2 \sin^2 \theta} + \lambda_d \cos \theta \right)$  (Holtzman & Segre, 2015) is introduced to represent the occurrence of burst mode (Figure 1j):

$$\delta P_{cr} \sim \frac{\sigma}{R_c} = \frac{\sigma}{\frac{a}{2} \cdot \left( \sqrt{1 - \lambda_d^2 \sin^2 \theta} + \lambda_d \cos \theta \right)}, \quad (3)$$

where  $\lambda_d$  is the microscopic characteristic length of the pore network,  $\lambda_d = \bar{d}/\bar{a}$ ,  $\bar{d}$  is the average diameter of the discoid-shaped grains and  $\bar{a}$  is the average spacing between their centers in the triangular lattices. In this study,  $\bar{d} = 570 \mu\text{m}$  and  $\bar{a} = 600 \mu\text{m}$ .

The transition from fingering to stable flow indicates that the magnitude of  $\delta P_v$  is the same as  $\delta P_{cr}$ :

$$|\delta P_v| = \delta P_{cr}. \quad (4)$$

Since the permeability  $K$  and the distance  $\delta x$  can be respectively scaled by  $K \sim a^2$ , and  $\delta x \sim a$  (Blunt & Scher, 1995; Holtzman & Segre, 2015), substituting equations (2) and (3) into equation (4) with  $Ca = U\mu_i/\sigma$  yields the relation between critical capillary number  $Ca_c$  and the critical contact angle  $\theta_c$ :

$$\left(1 - \frac{1}{M}\right) Ca_c = \frac{2c_0}{\sqrt{1 - \lambda_d^2 \sin^2 \theta_c} + \lambda_d \cos \theta_c}, \quad (5)$$

where  $c_0$  is a coefficient. We determine  $c_0$  using a specific critical contact angle  $\theta_c^* \approx 75^\circ$  corresponding to the crossover point at a specific capillary number  $Ca_c^* \approx 10^{-5.04}$ , as supported by numerical evidence (bottom row in SI Figure S2). Substituting  $Ca_c^*$  and  $\theta_c^*$  into equation (5), we have

$$\frac{Ca_c}{Ca_c^*} = \frac{\sqrt{1 - \lambda_d^2 \sin^2 \theta_c^*} + \lambda_d \cos \theta_c^*}{\sqrt{1 - \lambda_d^2 \sin^2 \theta_c} + \lambda_d \cos \theta_c}. \quad (6)$$

Consequently, we obtain a theoretical model for capturing the transition from fingering to stable flow influenced by wettability and flow rate:

$$Ca_c = \lambda_0 \left( \sqrt{1 - \lambda_d^2 \sin^2 \theta_c} - \lambda_d \cos \theta_c \right), \quad (7)$$

where  $\lambda_0 = Ca_c^* / \left( \sqrt{1 - \lambda_d^2 \sin^2 \theta_c^*} - \lambda_d \cos \theta_c^* \right)$  is a parameter dependent on the microscopic characteristic length  $\lambda_d$ , the specific critical contact angle  $\theta_c^*$ , and the specific capillary number  $Ca_c^*$ , which are in turn dependent on the pore and pore network heterogeneity.

Figure 2 shows the boundary between fingering and stable flow regimes as a function of  $\theta$  and  $Ca$  described by equation (7) with  $\lambda_d = 0.95$  (solid curve). Note that, unity for nonoverlapping disks. Larger pore body-throat aspect ratios correspond to higher  $\lambda_d$  (closer to 1). In this study, the overlapping disks induce “dead” pores and thus increase the permeability contrast, and eventually the value of  $\lambda_d$  should be larger than 0.95 which is originally defined for the nonoverlapping pore network (Holtzman & Segre, 2015). Figure 2a shows that  $\lambda_d = 0.99$  could well describe the boundary between the crossover zone and the stable flow. As shown in Figure 2, the region between  $\lambda_d = 0.95$  (solid curve) and  $\lambda_d = 0.99$  (dashed curve) well captures the crossover from fingering to stable flow regimes. For any point above the dashed curve, the viscous pressure drop stabilizing the displacement front is dominant over the capillary force (Figure 2b), whereas for the points below the solid curve, the burst events at local scale control the fluid invasion processes and the flow exhibits capillary fingering (Figure 2d). The effects of viscous force and capillary force are comparable in the regime between the two curves, which results in the crossover from fingering to stable flow (Figure 2c).

### 3. Phase Diagram With Corner Flow

The phase diagram (Figure 2) proposed by the scaling analysis in the 2-D system does not account for corner flow. Under very slow flow rate conditions, if  $\theta < 90^\circ - \alpha/2$  (Concus & Finn, 1969), where  $\alpha$  is the corner angle (here  $\alpha = 90^\circ$ ), the invading fluid advances in the corners where the posts touch the bottom and top surfaces, known as corner flow (Dong & Chatzis, 2004; Ransohoff & Radke, 1988). Experimental investigations show that the precursor wetting films move ahead of the primary displacement front (Dong & Chatzis, 2010; Tzimas et al., 1997; Vizika & Payatakes, 1989; Vizika et al., 1994). The length of the wetting film in the corner ( $l_{cor}$ ), defined as the distance between the wetting film tip and the primary front tip and determined from the invading fluid distribution (supporting information Figure S6), decreases with increasing  $Ca$  and  $\theta$ . Specifically, when  $Ca$  approaches up to a critical value  $Ca_{cf}$ , corner flow vanishes and  $l_{cor}$  is comparable to or smaller than the diameter of the post (i.e.,  $l_{cor}/d_0 \leq 1$ ) (Tzimas et al., 1997; Vizika & Payatakes, 1989). This critical capillary number  $Ca_{cf}$  is evidently a function of contact angle  $\theta$ , that is,  $Ca_{cf} = Ca_{cf}(\theta)$ .

To extend the above phase diagram from  $\theta = 45^\circ$  down to  $\theta = 5^\circ$  with consideration of corner flow, we numerically determine the relation between  $Ca_{cf}$  and  $\theta$ . Since the scale of wetting film is microscale or even nanoscale (Tokunaga, 2012) and numerical simulation is mesh dependent, we first determine the reasonable mesh size by validating numerical results with analytical solutions in a  $40 \mu\text{m}$  square capillary tube (Dong & Chatzis, 1995). The simulation shows that numerical results with mesh size of  $2 \mu\text{m}$  can reasonably reproduce the analytical results (supporting information Figure S3). We then perform pore-scale simulation with mesh size of  $2 \mu\text{m}$  in a subdomain ( $2.2 \text{ mm} \times 1.6 \text{ mm} \times 40 \mu\text{m}$ ) selected from the pore network, with a total of 8,581,760 cells and 9,368,224 points (supporting information Figure S4).

Figures 3a–3l show the phase distribution of invading fluid (brine) when the tip of front touches the outlet of the subdomain. For the lowest  $Ca$  ( $\log_{10} Ca = -5.04$ ) and the smallest  $\theta$  ( $\theta = 5^\circ$ ) shown in Figure 3i, the wetting film advances ahead of the primary front along the corners formed by the posts and the top/bottom surfaces (Figure 3i; supporting information Movie S1), which agrees with microfluidic experimental observations (Zhao, 2017; Zhao et al., 2016). Note that since the posts are nonoverlapping in the subdomain considered, the wetting films connect from post to post on the boundary (see supporting information Figure S5 and Movie S1). Figures 3a–3l also suggests that corner flow is suppressed by increasing  $Ca$  and  $\theta$  (supporting information Movies S2 and S3). To quantify the occurrence of corner flow, we plot the variations of the normalized wetting film length  $l_{cor}/d_0$  with  $Ca$  and  $\theta$  (Figure 3m). It shows that the contour of  $l_{cor}/d_0 = 1$  roughly follows a linear trend. As an approximation, we characterize the trend by

$$\log_{10} Ca_{cf} = \lambda_c \theta + b_c. \quad (8)$$

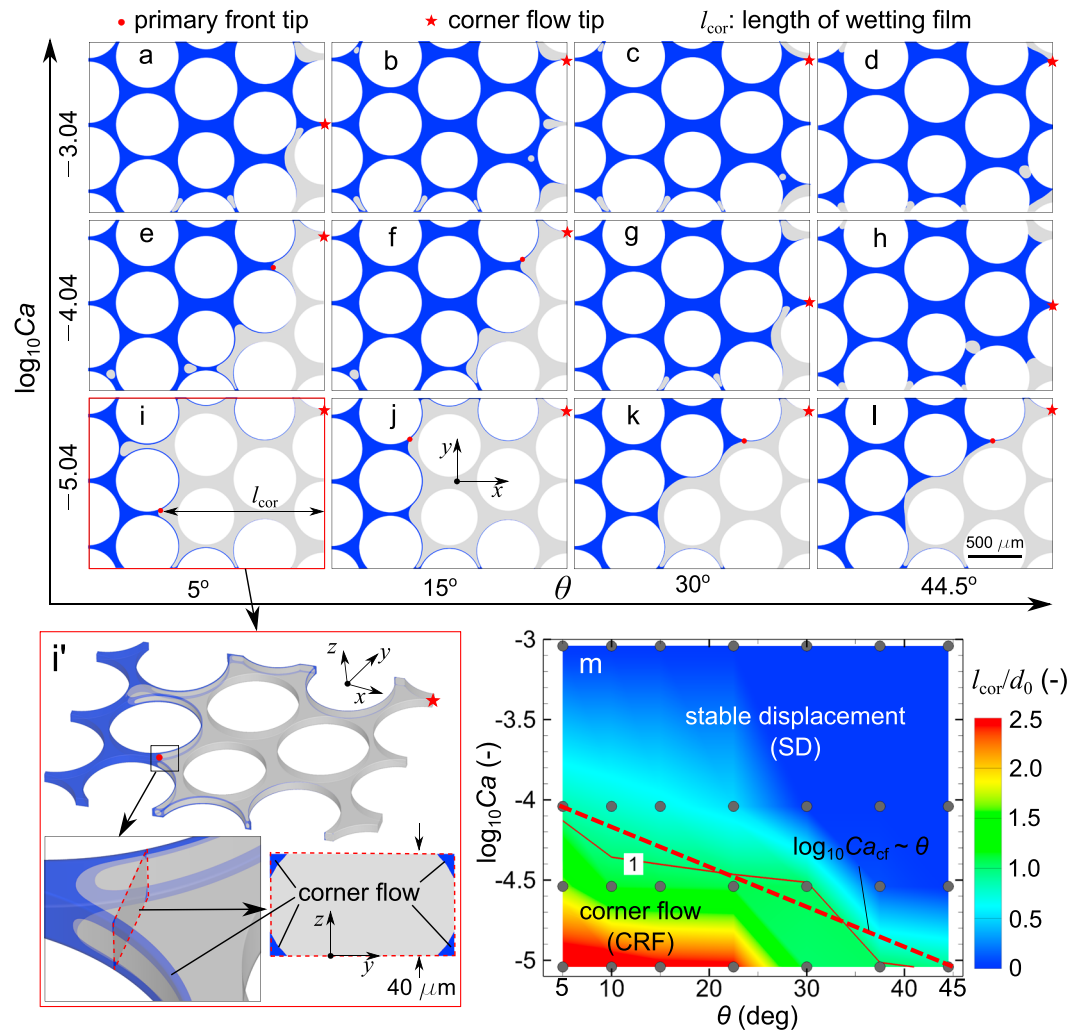


**Figure 3.** Corner flow and cooperative filling. (a–l) The 2-D distribution of invading fluid at the time when the front tip reaches the outlet of the subdomain. The invading fluid contact angle  $\theta$  increases from left to right, while the flow rate (or  $\log_{10} Ca$ ) increases from bottom to top. The blue color is brine and the gray is  $scCO_2$ . The primary displacement front tip and the wetting film tip are respectively denoted by circle and pentagram. (i) The distance between the wetting film tip and the primary front tip,  $l_{cor}$ , can be easily determined from the simulated phase distribution, and the details are shown in supporting information Figure S6. (i') The 3-D distribution of the invading phase. Under strong imbibition ( $\theta = 5^\circ$ ) and slow flow rate ( $\log_{10} Ca = -5.04$ ) conditions, precursor wetting films form and advance in the corners, ahead of the primary front. (m) The variation of the normalized wetting film length  $l_{cor}/d_0$  with  $Ca$  and  $\theta$ . Black dots represent 28 numerical simulations. The isoline of  $l_{cor}/d_0 = 1$  (solid line) shows the occurrence of corner flow. The log of the critical capillary number decreases roughly linearly with  $\theta$ .

The expression of  $Ca_{cf}(\theta)$  is determined by assigning  $\log_{10} Ca_{cf}(5^\circ) = -4.04$  and  $\log_{10} Ca_{cf}(45^\circ) = -5.04$ , leading to  $\lambda_c = -0.025$  and  $b_c = -3.915$ . We will show below that this approximate relation is supported by experiments shown in Figure 4. A more accurate relation, however, needs further investigation.

The empirical relation given by equation (8) indicates that for  $Ca > Ca_{cf}(\theta)$ , corner flow vanishes, and cooperative filling of multiple neighboring menisci dominates the displacement processes. But as  $Ca$  gradually increases beyond a limit  $Ca_{ic}$ , the pore-scale displacement becomes incomplete, that is, the defending fluid is partially displaced behind the displacement front. For unfavorable case of  $M < 1$ , the invading fluid advances along the top and bottom surfaces with thin films under strong imbibition conditions ( $\theta \approx 7^\circ$ ) (Levaché & Bartolo, 2014), whereas it advances along the center between the top and bottom surfaces under strong drainage conditions ( $\theta \approx 150^\circ$ ) (Zhao, 2017; Zhao et al., 2016). On the other hand, for favorable case  $M > 1$  considered in this paper, the invading fluid phase only moves along the center regardless of  $\theta$  (Chan et al., 2013) if  $Ca > Ca_{ic}$ . To obtain the critical capillary number  $Ca_{ic}$  that corresponds to the occurrence of the incomplete



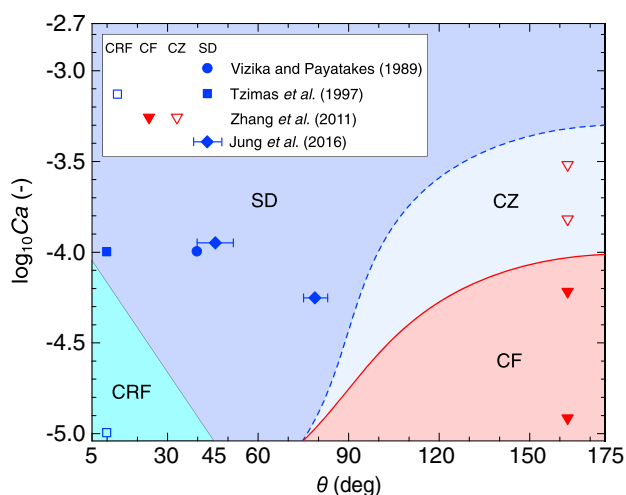


**Figure 4.** Phase diagram in the  $\theta$ - $\log_{10}Ca$  plane depicting the crossover (CZ) from capillary fingering (CF) to stable displacement (SD) ( $45^\circ \leq \theta \leq 175^\circ$ ) and the boundary between corner flow (CRF) and stable displacement (or cooperative filling) ( $5^\circ \leq \theta < 45^\circ$ ) under favorable displacement conditions. Four experiment data sets (Jung et al., 2016; Tzimas et al., 1997; Vizika & Payatakes, 1989; Zhang et al., 2011) are selected to evaluate the proposed phase diagram. For  $45^\circ \leq \theta \leq 175^\circ$ , the crossover from capillary fingering to stable displacement is predicted by our theoretical model (equation (7)). Note that in the experiments of Zhang et al. (2011) (open and solid triangles), the post diameter is  $300 \mu\text{m}$  and the pore throat's size is  $40 \mu\text{m}$ , resulting in a characteristic length  $\lambda_d = \bar{d}/\bar{a} = 0.938$  (red solid curve). The dashed curve corresponds to the characteristic length  $\lambda_d = 0.99$ , also shown in Figure 2. Under conditions of  $5^\circ \leq \theta < 45^\circ$ , the boundary between corner flow and stable displacement (cooperative filling) is given by equation (8). The horizontal bars of the values by Jung et al. (2016) indicate standard deviations of contact angle measurements.

wetting films were observed at  $\log_{10}Ca = -4$  (solid square). The experiments by Vizika and Payatakes (1989) also show that favorable displacement pattern is stable at  $\theta = 40^\circ$  and  $\log_{10}Ca = -4$  (solid circle). Recently, Jung et al. (2016) reported that for water-air system under conditions of  $\theta = 46^\circ$ ,  $\log_{10}Ca = -3.96$  and  $\theta = 79^\circ$ ,  $\log_{10}Ca = -4.25$ , stable fronts were observed (solid diamond). In summary, the phase diagram boundaries given by equations (7) and (8) generally capture the displacement patterns observed in existing experiments. Note that although the location of the boundaries for different patterns is dependent on the pore structure and the roughness of the pore surface (Dullien, 1992), the phase diagram provides a general picture for the pattern formations jointly influenced by wettability and flow rate.

#### 4. Conclusions

We proposed a theoretical model to elucidate the competing effects of wettability and flow rate on the displacement patterns. The phase diagram predicted by the theoretical model describes the crossover from fingering to stable flow regimes with consideration of wettability, and therefore, extends the classic phase diagram (Lenormand, 1990; Lenormand et al., 1988; Zhang et al., 2011) to consider the wettability within the range from strong imbibition ( $\theta = 5^\circ$ ) to strong drainage ( $\theta = 175^\circ$ ). Our phase diagram also captures the crossover from corner flow to cooperative filling (stable displacement) under strong imbibition conditions ( $5^\circ \leq \theta < 45^\circ$ ). Thus, our work extends the previous studies about the wettability effect on displacement patterns in the capillary-dominated flow regime (Cieplak & Robbins, 1988, 1990; Jung et al., 2016). Our work bridges understanding of menisci advancement at the pore scale and displacement front instability at the pore network scale, providing not only an insight into the effects of wettability and flow rate, but also a basis for an upscaling methodology that directly relates Darcy scale flow parameters to menisci dynamics (Armstrong et al., 2016). This analysis could become of practical significance for geologic carbon sequestration

displacement, we solve a four-dimensional dynamical system for the force-balance equation that describes the meniscus shape with various  $Ca$  and  $\theta$  values (supporting information Figure S7). As  $Ca$  increases up to a critical value ( $Ca_{ic}$ ), no stationary solution is obtained (Levaché & Bartolo, 2014), indicating the occurrence of incomplete displacement. The numerical solutions show that  $Ca_{ic}$  decreases with  $\theta$ , approaching a minimum of  $\log_{10}Ca_{ic} = -2.30$  at  $\theta = 175^\circ$  (supporting information Figures S8 and S9). The minimum of  $Ca_{ic}$  is larger than the maximum  $Ca$  in Figure 2, indicating that the incomplete displacement cannot occur in the domain of stable displacement considered in this study ( $\log_{10}Ca < -2.74$ ).

The above discussion not only extends the phase diagram to strong imbibition ( $\theta = 5^\circ$ ) with the inclusion of a corner flow regime but also provides a constraint for the proposed theoretical model (equation (7)) that  $Ca$  should be no more than  $Ca_{ic}(\theta)$ . Figure 4 presents the extended phase diagram for the full range of  $\theta$ , which integrates theoretical crossover from fingering to stable flow regimes (equation (7)) and the empirical boundary between corner flow and stable displacement (equation (8)).

We evaluate the proposed phase diagram using available experimental data. Since the experimental data under favorable conditions, including immiscible displacements with various wetting conditions and flow rates is rather limited in the literature, only four data sets were selected herein. Under drainage condition, Zhang et al. (2011) conducted a series of experiments for  $M > 1$ , showing that for a specific contact angle  $\theta = 163^\circ$ , the displacement patterns at  $\log_{10}Ca = -4.92$  and  $\log_{10}Ca = -4.22$  are capillary fingering (solid triangle in Figure 4), whereas for higher  $Ca$  ( $\log_{10}Ca = -3.82$  and  $\log_{10}Ca = -3.52$ ) the patterns are the crossover from fingering to stable displacement (open triangle), which can be captured by our proposed phase diagram. In experiments by Tzimas et al. (1997), for  $M > 1$  at  $\theta = 10^\circ$ , wetting films were observed at  $\log_{10}Ca = -5$  with length  $l_{cor}/d_0 \approx 1-2$ , which represents corner flow (open square), whereas no

and enhanced gas recovery through targeting desirable regions in the phase diagram by adjusting injection rates and potentially the wettability to enhance either capillary trapping or displacement efficiency.

#### Acknowledgments

This work is supported by the National Natural Science Foundation of China (grants 51779188 and 51579188), and also funded by the Center for Nanoscale Control of Geologic CO<sub>2</sub> (NCGC), an Energy Frontier Research Center (EFRC) of the U.S. Department of Energy, Office of Science, Office of Basic Energy Sciences under award DE-AC02-05CH11231. The numerical calculations in this study were done on the supercomputing system in the Supercomputing Center of Wuhan University. Data and images supporting this paper can be found in the supporting information. We thank Ruben Juanes and an anonymous reviewer for their critical reviews and suggestions. We also thank Lichun Wang for valuable suggestions.

#### References

- Anderson, R., Zhang, L., Ding, Y., Blanco, M., Bi, X., & Wilkinson, D. P. (2010). A critical review of two-phase flow in gas flow channels of proton exchange membrane fuel cells. *Journal of Power Sources*, *195*(15), 4531–4553.
- Anderson, W. G. (1986). Wettability literature survey part 2: Wettability measurement. *Journal of Petroleum Technology*, *38*(11), 1246–1262.
- Armstrong, R. T., McClure, J. E., Berrill, M. A., Rücker, M., Schlüter, S., & Berg, S. (2016). Beyond Darcy's law: The role of phase topology and ganglion dynamics for two-fluid flow. *Physical Review E*, *94*(4-1), 043113.
- Benson, S. M., & Cole, D. R. (2008). CO<sub>2</sub> sequestration in deep sedimentary formations. *Elements*, *4*(5), 325–331.
- Blunt, M. J., & Scher, H. (1995). Pore-level modeling of wetting. *Physical Review E*, *52*(6), 6387.
- Cao, S. C., Dai, S., & Jung, J. (2016). Supercritical CO<sub>2</sub> and brine displacement in geological carbon sequestration: Micromodel and pore network simulation studies. *International Journal of Greenhouse Gas Control*, *44*, 104–114.
- Chan, T. S., Srivastava, S., Marchand, A., Andreotti, B., Biferale, L., Toschi, F., et al. (2013). Hydrodynamics of air entrainment by moving contact lines. *Physics of Fluids*, *25*(7), 42–459.
- Chapuis, O., Prat, M., Quintard, M., Chane-Kane, E., Guillot, O., & Mayer, N. (2008). Two-phase flow and in model fibrous media: Application to the gas diffusion layer of PEM fuel cells. *Journal of Power Sources*, *178*(1), 258–268.
- Chaudhary, K., Cardenas, M. B., Wolfe, W. W., Maisano, J. A., Ketcham, R. A., & Bennett, P. C. (2013). Pore-scale trapping of supercritical CO<sub>2</sub> and the role of grain wettability and shape. *Geophysical Research Letters*, *40*, 3878–3882. <https://doi.org/10.1002/grl.50658>
- Chen, Y.-F., Fang, S., Wu, D.-S., & Hu, R. (2017). Visualizing and quantifying the crossover from capillary fingering to viscous fingering in a rough fracture. *Water Resources Research*, *53*, 7756–7772. <https://doi.org/10.1002/2017WR021051>
- Chraïbi, H., Prat, M., & Chapuis, O. (2009). Influence of contact angle on slow evaporation in two-dimensional porous media. *Physical Review E*, *79*(2 Pt 2), 026313.
- Cieplak, M., & Robbins, M. O. (1988). Dynamical transition in quasistatic fluid invasion in porous media. *Physical Review Letters*, *60*(20), 2042–2045.
- Cieplak, M., & Robbins, M. O. (1990). Influence of contact angle on quasistatic fluid invasion of porous media. *Physical Review B*, *41*(41), 11508–11521.
- Concus, P., & Finn, R. (1969). On the behavior of a capillary surface in a wedge. *Proceedings of the National Academy of Sciences of the United States of America*, *63*(2), 292–299.
- Dong, M., & Chatzis, I. (1995). The imbibition and flow of a wetting liquid along the corners of a square capillary tube. *Advances in Colloid and Interface Science*, *172*(2), 278–288.
- Dong, M., & Chatzis, I. (2004). An experimental investigation of retention of liquids in corners of a square capillary. *Advances in Colloid and Interface Science*, *273*(1), 306–312.
- Dong, M., & Chatzis, I. (2010). Effect of capillary pressure on wetting film imbibition ahead of main liquid-gas displacement front in porous media. *Petroleum Science and Technology*, *28*(9), 955–968.
- Dullien, F. A. L. (1992). *Porous media: Fluid transport and pore structure*. San Diego, CA: Academic Press.
- El-Maghraby, R. M., & Blunt, M. J. (2013). Residual CO<sub>2</sub> trapping in Indiana limestone. *Environmental Science & Technology*, *47*(1), 227–233.
- Greenshields, C. (2015). OpenFOAM user guide. *OpenFOAM Foundation Ltd*.
- He, S., Kahanda, G. L., & Pz, W. (1992). Roughness of wetting fluid invasion fronts in porous media. *Physical Review Letters*, *69*(26), 3731–3734.
- Herring, A. L., Andersson, L., Schlüter, S., Sheppard, A., & Wildenschild, D. (2015). Efficiently engineering pore-scale processes: The role of force dominance and topology during nonwetting phase trapping in porous media. *Advances in Water Resources*, *79*, 91–102.
- Holtzman, R., & Segre, E. (2015). Wettability stabilizes fluid invasion into porous media via nonlocal, cooperative pore filling. *Physical Review Letters*, *115*(6), 164501.
- Homsy, G. M. (1987). Viscous fingering in porous media. *Annual Review of Fluid Mechanics*, *19*(1), 271–311.
- Hu, R., Wan, J., Kim, Y., & Tokunaga, T. K. (2017a). Wettability impact on supercritical CO<sub>2</sub> capillary trapping: Pore-scale visualization and quantification. *Water Resources Research*, *53*, 6377–6394. <https://doi.org/10.1002/2017WR020721>
- Hu, R., Wan, J., Kim, Y., & Tokunaga, T. K. (2017b). Wettability effects on supercritical CO<sub>2</sub>-brine immiscible displacement during drainage: Pore-scale observation and 3D simulation. *International Journal of Greenhouse Gas Control*, *60*, 129–139.
- Iglauer, S., Pentland, C. H., & Busch, A. (2015). CO<sub>2</sub> wettability of seal and reservoir rocks and the implications for carbon geo-sequestration. *Water Resources Research*, *51*, 729–774. <https://doi.org/10.1002/2014WR015553>
- Jamaloei, B. Y., Asghari, K., & Kharrat, R. (2012). The investigation of suitability of different capillary number definitions for flow behavior characterization of surfactant-based chemical flooding in heavy oil reservoirs. *Journal of Petroleum Science and Engineering*, *90*-91(7), 48–55.
- Jung, M., Brinkmann, M., Seemann, R., Hiller, T., Lama, M. S. D. L., & Herminghaus, S. (2016). Wettability controls slow immiscible displacement through local interfacial instabilities. *Physical Review Fluids*, *1*, 074202.
- Kim, Y., Wan, J., Kneafsey, T. J., & Tokunaga, T. K. (2012). Dewetting of silica surfaces upon reactions with supercritical CO<sub>2</sub> and brine: Pore-scale studies in micromodels. *Environmental Science & Technology*, *46*(7), 4228–4235.
- Koiller, B., Hong, J., & Robbins, M. O. (1992). Fluid wetting properties and the invasion of square networks. *Physical Review B*, *45*(14), 7762–7767.
- Lenormand, R. (1990). Liquids in porous media. *Journal of Physics: Condensed Matter*, *2*(S), SA79–SA88.
- Lenormand, R., Touboul, E., & Zarcone, C. (1988). Numerical models and experiments on immiscible displacements in porous media. *Journal of Fluid Mechanics*, *189*(1), 165–187.
- Levaché, B., & Bartolo, D. (2014). Revisiting the Saffman-Taylor experiment: Imbibition patterns and liquid-entrainment transitions. *Physical Review Letters*, *113*(4), 044501.
- Mason, G., & Morrow, N. R. (2013). Developments in spontaneous imbibition and possibilities for future work. *Journal of Petroleum Science and Engineering*, *110*, 268–293.
- Philip, J. R. (1971). Limitations on scaling by contact angle. *Soil Science Society of America Journal*, *35*(3), 507–509.
- Ransohoff, T. C., & Radke, C. J. (1988). Laminar flow of a wetting liquid along the corners of a predominantly gas-occupied noncircular pore. *Journal of Colloid and Interface Science*, *121*(2), 392–401.
- Singh, K., Scholl, H., Brinkmann, M., Michiel, M. D., Scheel, M., Herminghaus, S., et al. (2017). The role of local instabilities in fluid invasion into permeable media. *Scientific Reports*, *7*(1), 444.

- Tokunaga, T. K. (2012). DLVO-based estimates of adsorbed water film thicknesses in geologic CO<sub>2</sub> reservoirs. *Langmuir*, 28(21), 8001–8009.
- Trojer, M., Szulczewski, M. L., & Juanes, R. (2015). Stabilizing fluid-fluid displacements in porous media through wettability alteration. *Physical Review Applied*, 3(5), 054008.
- Tsuji, T., Jiang, F., & Christensen, K. T. (2016). Characterization of immiscible fluid displacement processes with various capillary numbers and viscosity ratios in 3D natural sandstone. *Advances in Water Resources*, 95, 3–15.
- Tzimas, G. C., Matsuura, T., Avraam, D. G., Der Bruggen, W. V., Constantinides, G. N., & Payatakes, A. C. (1997). The combined effect of the viscosity ratio and the wettability during forced imbibition through nonplanar porous media. *Journal of Colloid and Interface Science*, 189(1), 27–36.
- Vizika, O., & Payatakes, A. C. (1989). Parametric experimental study of forced imbibition in porous media. *Physicochemical Hydrodynamics*, 11(1), 187–204.
- Vizika, O., Avraam, D. G., & Payatakes, A. C. (1994). On the role of the viscosity ratio during low-capillary-number forced imbibition in porous media. *Advances in Colloid and Interface Science*, 165(2), 386–401.
- Wong, P. (1994). Flow in porous media: Permeability and displacement patterns. *MRS Bulletin*, 19(05), 32–38.
- Yamabe, H., Tsuji, T., Liang, Y., & Matsuoka, T. (2015). Lattice Boltzmann simulations of supercritical CO<sub>2</sub>-water drainage displacement in porous media: CO<sub>2</sub> saturation and displacement mechanism. *Environmental Science & Technology*, 49(1), 537–543.
- Zhang, C., Oostrom, M., Wietsma, T. W., Grate, J. W., & Warner, M. G. (2011). Influence of viscous and capillary forces on immiscible fluid displacement: Pore-scale experimental study in a water-wet micromodel demonstrating viscous and capillary fingering. *Energy & Fuels*, 25(8), 3493–3505.
- Zhao, B. (2017). Multiphase flow in porous media: The impact of capillarity and wettability from field-scale to pore-scale (PhD thesis). Massachusetts Institute of Technology.
- Zhao, B., Macminn, C. W., & Juanes, R. (2016). Wettability control on multiphase flow in patterned microfluidics. *Proceedings of the National Academy of Sciences of the United States of America*, 113(37), 10,251–10,256.
- Zheng, X., Mahabadi, N., Yun, T. S., & Jang, J. (2017). Effect of capillary and viscous force on CO<sub>2</sub> saturation and invasion pattern in the microfluidic chip. *Journal of Geophysical Research: Solid Earth*, 122, 1634–1647. <https://doi.org/10.1002/2016JB013908>